Dynamic Nonprehensile Manipulation for Rotating a Thin Deformable Object: an Analogy to Bipedal Gaits

Ixchel G. Ramirez-Alpizar, *Student Member, IEEE,* Mitsuru Higashimori, *Member, IEEE,* Makoto Kaneko, *Fellow, IEEE,* Chia-Hung Dylan Tsai, *Member, IEEE,* and Imin Kao, *Member, IEEE*

***Abstract*—A rigid plate end-effector at the tip of a high-speed manipulator can remotely manipulate an object without grasping it. This paper discusses a dynamic nonprehensile manipulation strategy for rotating thin deformable objects on a rigid plate with two degrees of freedom. The deformation of the object due to dynamic effects is exploited to produce fast and stable rotation. By varying the frequency of the rotational component of the plate's motion, we show that the dynamic behavior of the object mimics either a sliding, walking, or running gait of a biped. We introduce a model to simulate this type of system in which the object is constructed of multiple nodes connected by viscoelastic joint units with three degrees of freedom. The joint's viscoelastic parameters are estimated experimentally in order to model real food. Afterward, simulation analysis is used to investigate how the object's rotational behavior and its angular velocity change with respect to the plate's motion frequency. We show how the object's behavior during rotation is analogous to bipedal sliding, walking, and running gaits, and then obtain optimal plate motions leading to the maximal angular velocity of the object. We also reveal that an appropriate angular acceleration of the plate is essential for a dynamically stable and fast object's rotation. We further show that the friction coefficient that maximizes the object's angular velocity depends on its gait.**

***Index Terms*—Nonprehensile manipulation, dynamic skill, deformable object.**

I. Introduction

ADVANCEMENT in technology has allowed the development of dynamic skills in robots, which in recent years has attracted many researchers [1], [2]. In the particular case where a simple end-effector is used, a robot-system can compensate for its lack of degrees of freedom (DOFs) and sensors by utilizing dynamic effects produced by high-speed robot motions and by using an appropriate manipulation strategy [3]–[15].

Arai *et al.* have discussed a manipulation strategy where a cube is rotated around its edge on a plate attached at the tip of a six DOFs manipulator [3]. Lynch *et al.* have examined the juggling skill called "Butterfly," where a ball is transported along the inside and the outside of a palm surface, and discussed the shape of the robot palm and motion planning [4]. Lynch *et al.* have discussed controllability, motion planning, and implementation of planar dynamic nonprehensile manipulation [5]. Various dynamic tasks were performed by using a single joint manipulator. Those tasks include snatching an object from a table, rolling an object on the surface of an arm, and throwing and catching it. Amagai *et al.* have shown the experiments where an object is manipulated on a plate attached at the tip of a six DOFs manipulator based on visual information [6]. Reznik and Canny have developed the Universal Planar Manipulator (UPM) based on a single horizontally-vibrating plate with three DOFs [7]–[9]. They have demonstrated that multiple objects were simultaneously moved toward target directions. Böhringer *et al.* have developed a model for the mechanics of microactuators together with a sensorless parallel manipulation theory [10] and have discussed algorithms for sensorless positioning and orienting of planar parts using different vibration patterns [11]. They also proposed microassembly of parts using ultrasonic vibration and electrostatic forces to position and align parts in parallel on a vibratory table [12]. Vose *et al.* have discussed sensorless control methods for point parts sliding on a rigid plate. They have estimated the programmable velocity fields for point parts and shown basic experiments by using a six DOFs vibrating plate [13]. They have also shown that translation and rotation of a rigid plate induces parts on the plate to move toward or away from a nodal line aligned with the rotation axis [14], and how to find frictional velocity fields generated by plate motions [15]. These works done on manipulation utilizing a plate have supposed that the object is a particle(s) or a rigid body(ies) since it is convenient from the viewpoint of both geometric and dynamic analysis. In contrast, conventional works treating a deformable object have generally supposed two or more fingers for grasping and handling the object [16]–[23]. As far as we know, there are no works dealing with a deformable object as the main target in nonprehensile manipulation.

Our former works treated a dynamic manipulation inspired by the handling of a pizza peel [24], as shown in Fig. 1(a). A chef handles the peel and remotely manipulates a pizza on the plate. We found that the chef aggressively utilizes two DOFs from the remote handling location during the manipulation: translation X along the bar and rotation Θ around the bar. We proposed a dynamic nonprehensile manipulation

The materials in this paper were presented in part at the IEEE International Conference on Robotics and Automation, Shanghai, China, May 2011.

I. G. Ramirez-Alpizar, M. Higashimori, M. Kaneko, and C. D. Tsai are with the Department of Mechanical Engineering, Graduate School of Engineering, Osaka University, 2-1 Yamadaoka, Suita, 565-0871, Japan (email: ixchel@hh.mech.eng.osaka-u.ac.jp; higashi@mech.eng.osaka-u.ac.jp; mk@mech.eng.osaka-u.ac.jp; tsai@hh.mech.eng.osaka-u.ac.jp).

I. Kao is with the Department of Mechanical Engineering, State University of New York (SUNY) at Stony Brook, Stony Brook, NY 11794-2300, USA (email: ikao@ms.cc.sunysb.edu).

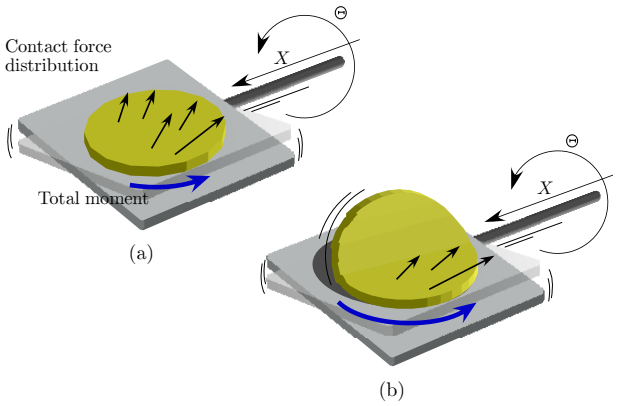

Fig. 1. Dynamic nonprehensile manipulation for rotating: (a) a rigid body and (b) a deformable body. The object's deformation generated by dynamic effects as shown in (b), can decrease the negative moment. As a result, the object can rotate faster.

for controlling the position and the orientation of a rigid object on a plate by applying the peel mechanism to the robot system. This manipulation scheme has the advantage that the robot can remotely manipulate an object in areas with high temperature, high humidity, electromagnetic field, etc, where a gripper or a robot hand with electronic/electrical/precision device(s) is unavailable. Furthermore, since the object is not grasped or picked, the concentration of stress inducing the object's destruction is avoided. We have also found that a deformable object can rotate faster than a rigid one [25], [26], as shown in Fig. 1(a) and (b). In order to extend the aforementioned investigation, in this paper we clarify what actually happens in the manipulation for rotating deformable objects. This paper explores the optimal conditions which includes the plate's motion, the object's physical properties and the friction between them.

In this paper, after showing the principle of rotating an object and some basic experiments, we introduce a simulation model in order to approximate the dynamic characteristics of a thin deformable object on the plate. This model is composed of multiple nodes with mass, where neighboring nodes are connected to each other by what we call a viscoelastic joint unit. This unit is composed of three joints: bending, compression/tension, and torsion. The bending and the compression joints have viscoelastic elements, while the torsion joint is free. After estimating the viscoelastic parameters of a slice of cheese as a sample of real food, we show the simulation results where the dynamic behavior of the object nicely corresponds to that in experiments. Through simulation analysis, we show that the object's rotational behavior changes with respect to the plate's motion frequency in a way that is similar to a biped transitioning from a sliding to a walking to a running gait. We also reveal that an optimal point leading to the maximal angular velocity of the object exists and depends upon the angular acceleration of the plate. Finally, we further investigate how the friction between the plate and the object influences the object's angular velocity and show that the optimal friction coefficient depends on the object's gait.

This paper is organized as follows. In section II, we explain the essence of the principle of rotation and show a basic

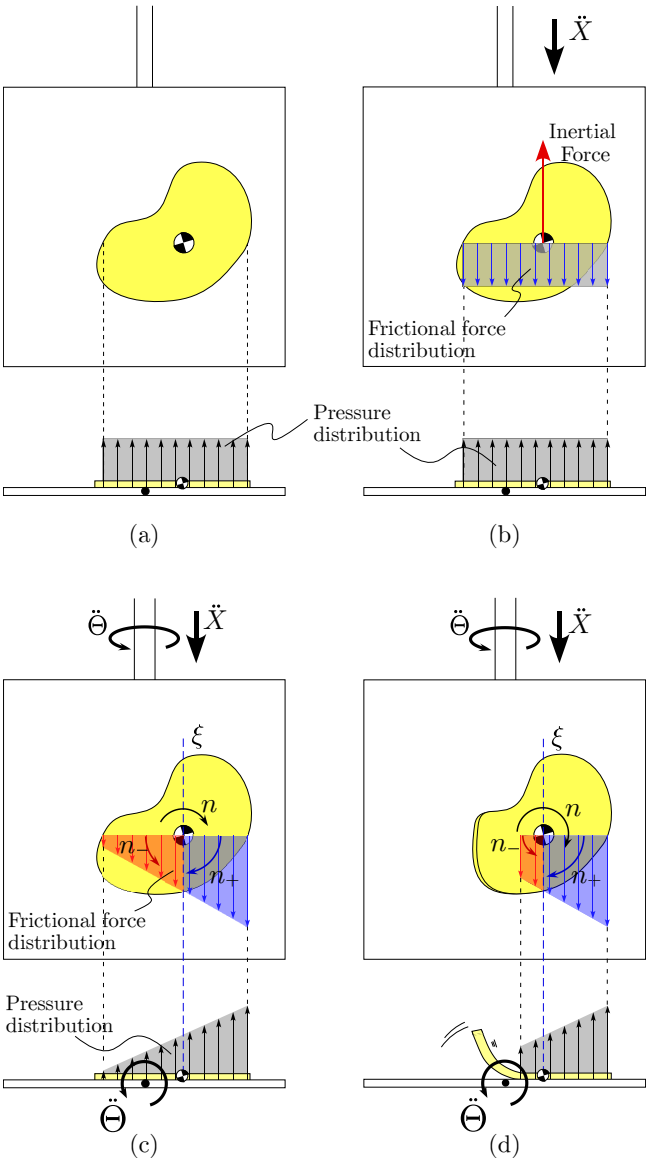

Fig. 2. Rotation mechanism: (a) Both the plate and the object are stationary, i.e. no motion is given to the plate (b) Only a translational motion $\ddot{X}$ is given to the plate, (c) Both translational $\ddot{X}$ and rotational $\ddot{\Theta}$ motions are given to the plate, (d) Due to the object's deformation the contact area decreases.

experiment. In section III, we introduce a simulation model for a deformable object. In section IV, we show how to estimate the viscoelastic parameters of the object. In section V, we show the simulation analysis based on real food. In section VI, we give the conclusion of this work.

II. Manipulation Mechanism

A. Principle of Rotation

Fig. 2 shows the top view and the side view of the object on the plate, this plate has two DOFs: translation X along the bar and rotation Θ around the bar, as shown in Fig. 1(a). The object as well as the plate are stationary ($X = 0$, $\Theta = 0$) in Fig. 2(a). Then, as shown in Fig. 2(b), by giving a translational acceleration $\ddot{X}$ to the plate, an inertial force and a frictional force are generated. In this case the nominal

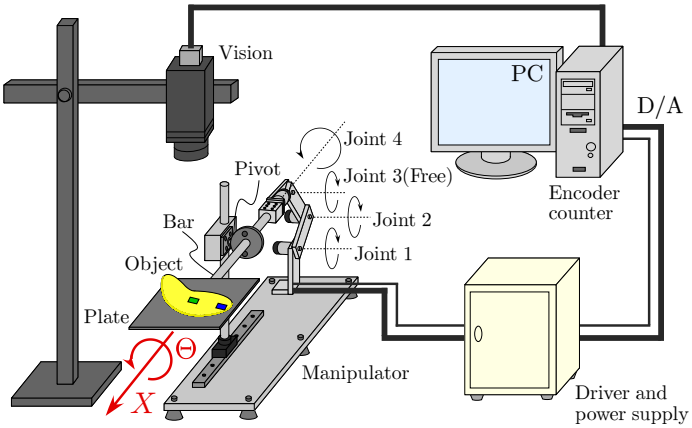

Fig. 3. Overview of the experimental system.

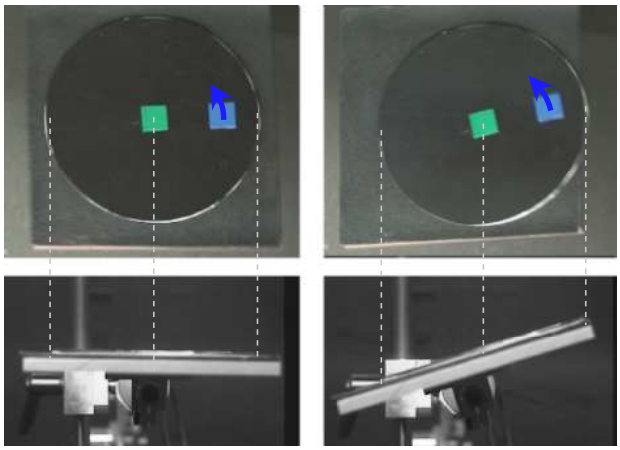

(a) $t = 0.14$[s] (b) $t = 0.54$[s]

Fig. 4. Rotational motion of a rigid object: the object is rotating with an angular velocity of 15.7 deg/s, for $A_p = 16$ deg.

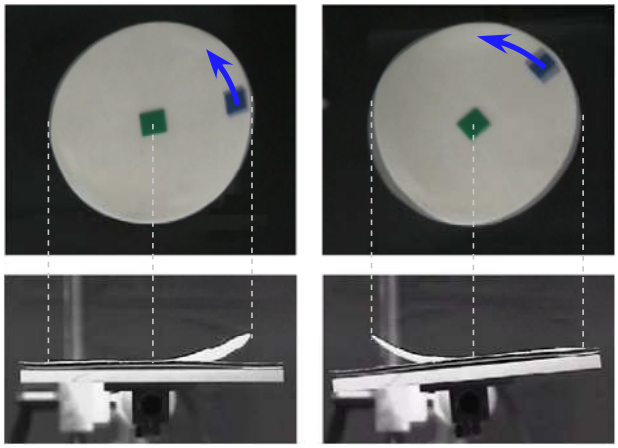

(a) $t = 0.14$[s] (b) $t = 0.52$[s]

Fig. 5. Rotational motion of a deformable object: the object is rotating with an angular velocity of 56.6 deg/s, for $A_p = 16$ deg.

pressure distribution on the object is assumed to be uniform and as a result the frictional force distribution is also uniform, as shown in Fig. 2(b), where we illustrate just the slice of the frictional force distribution that passes through the center of mass of the object. Let us now consider the case in which an angular acceleration $\ddot{\Theta}$ is additionally given to the plate, as shown in Fig. 2(c). In this instance, the pressure distribution on the object results in a slope due to the inertial force generated by $\ddot{\Theta}$, thus the frictional force distribution also slopes. A rotational moment n around the object's center of mass is generated by the slope in the frictional force, and therefore the object rotates. Let us consider that a line ξ which passes through the object's center of mass and runs parallel to the translational motion $\ddot{X}$, divides the rotational moment n into the moment contributing to rotation n_+ and the moment braking rotation n_-. In the case of a deformable object, as shown in Fig. 2(d), the inertial force generated by the plate's rotational motion produces a deformation in the object and as a result, the object's area in contact with the plate is reduced. Hence the moment braking rotation n_- decreases. From this reason it is thought that a deformable object rotates faster than a rigid one.

B. Basic Experiment

Fig. 3 shows an overview of the experimental system [24]. A plate is attached at the tip of a manipulator and a vision system observes the object on the plate. The manipulator possesses three active joints and a free joint. The plate of 100 mm $\times$ 100 mm fixed at the tip of the bar moves along the longitudinal axis of it (translational DOF: X) by the rotations of the 1st and the 2nd joints. The plate rotates around the longitudinal axis of the bar (rotational DOF: Θ) by the rotation of the 4th joint. A small circular pancake is utilized as a deformable object. It has a 10 g mass, a 42 mm radius, and a 1.0 mm thickness. Additionally, as a rigid body, we prepare another object made of plastic with the same physical properties except for the bending stiffness. We give to the plate's two DOFs of motion the sinusoidal trajectories given by $X(t) = 2\sin(14\pi t)$ mm and $\Theta(t) = -A_p \sin(14\pi t)$ deg[1]. The object rotates continuously on the plate by cyclically changing the frictional force distribution. Fig. 4 shows a series of photos of the rigid object's rotational motion, where the amplitude of Θ is given by $A_p = 16$ deg. From Fig. 4, it can be seen that the object does not bend and a full contact between the plate and the object is maintained. The object rotates with an angular velocity of 15.7 deg/s. Moreover, if we give an amplitude larger than $A_p = 16$ deg, the object becomes unstable and violently falls from the plate. On the contrary, Fig. 5 shows a series of photos of the deformable object's rotational motion, for the same plate's amplitude $A_p = 16$ deg. From Fig. 5, it can be seen that the object is bent by the inertial force given by the plate, thus the contact area between the plate and the

[1]From the initial state that the object is stationary, the rotational direction of the object is determined based on the plate's acceleration as follows: $\ddot{X}\ddot{\Theta} > 0$ generates the clockwise moment $n > 0$; while $\ddot{X}\ddot{\Theta} < 0$ generates the counterclockwise moment $n < 0$, as explained in [24]. If we assume the plate's motion is considerably faster than the object's one and since we give sinusoidal trajectories where the sign of $\ddot{X}\ddot{\Theta}$ is constant during the whole cycle, then the rotational direction of the object can be regarded as constant.

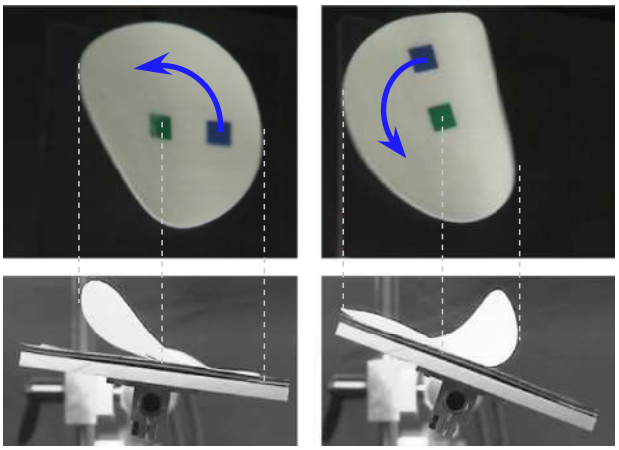

(a) $t = 0.21$[s] (b) $t = 0.61$[s]

Fig. 6. Rotational motion of a deformable object: the object is rotating with an angular velocity of 251 deg/s, for $A_p = 24$ deg.

object is decreased. This object's behavior works effectively for decreasing the brake moment, as explained in Fig. 2(d). As a result, the deformable object can rotate faster than the rigid one on the plate. The object rotates with an angular velocity of 56.6 deg/s, which is more than three times faster than the rigid object. Additionally, Fig. 6 shows a series of photos of the deformable object's rotational motion, where the amplitude of Θ is given by $A_p = 24$ deg. From Fig. 6, it can be seen that the object is bent even more than in Fig. 5, decreasing the contact area between the plate and the object to almost a half, decreasing the braking moment and thus rotating faster. In this case, the object rotates with an angular velocity of 251.7 deg/s.

III. Modeling

In preparation for the motion analysis we introduce a viscoelastic model for approximating dynamic behaviors of a thin deformable object on a plate.

Assumptions: Consider a plate and a thin deformable object as shown in Fig. 1(b). To simplify the analysis, we set the following assumptions:

1: The plate is rigid.
2: The plate's surface area is larger than that of the object.
3: The object is deformable and its thickness is small.
4: The object is isotropic and it has uniform mass distribution and uniform viscoelasticity.
5: The nominal pressure distribution on the object is uniform.
6: The friction coefficient between the plate and the object based on Coulomb's law is uniform and is given by μ_s and μ_k for static and dynamic coefficients, respectively.

Deformable object model: For a thin deformable object, we consider virtual tile links as shown in Fig. 7(a). The link is a square with sides of length l. Based on the shape and the size of the modeled object, the arrangement of virtual tiles is determined. A node with a mass of m is located at the center of the link, where neighboring nodes are connected to each other by a viscoelastic joint unit as shown in Fig. 7(b). The joint unit is composed of three DOFs: bending, compression/tension, and torsion. The bending and the compression joints have

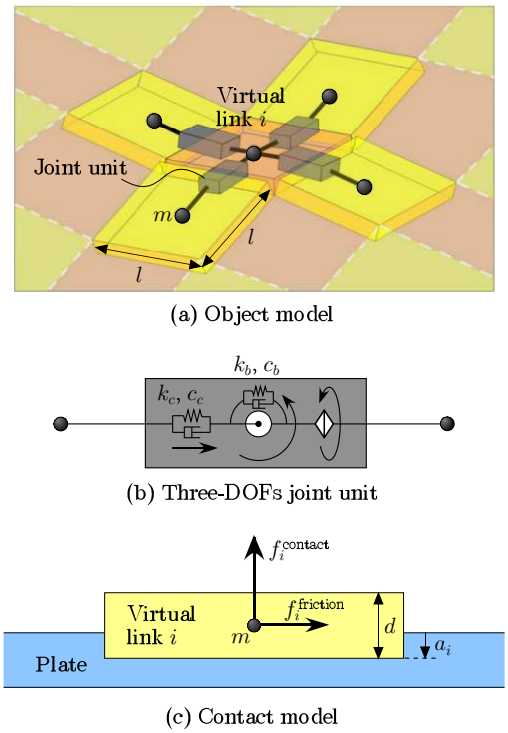

(a) Object model

(b) Three-DOFs joint unit

(c) Contact model

Fig. 7. Deformable object model.

viscoelastic elements given by a Kelvin-Voigt model, while the torsion joint is free for simplicity of the simulation model. In Fig. 7(b), k_b and c_b express the elasticity and viscosity, respectively, of the bending joint. Similarly, k_c and c_c are the elasticity and viscosity, respectively, of the compression joint.

Contact Model: Fig. 7(c) shows the contact model between the plate and the i-th virtual link. The contact force is computed with the penalty method based on the Kelvin-Voigt model [27]. The contact force f_i^{contact} applied to the node is given by

$$f_i^{\text{contact}} = k_{\text{contact}} a_i^{2.2} + c_{\text{contact}} \dot{a}_i \quad (a_i \geq 0) \tag{1}$$

where a_i, k_{contact}, and c_{contact} are the distance between the surface of the plate and that of the virtual link, the elasticity, and the viscosity, respectively. Also, the frictional force f_i^{friction} applied to the node is given by,

$$f_i^{\text{friction}} = \mu_* f_i^{\text{contact}}. \tag{2}$$

The coefficient of friction in (2) is defined by

$$\mu_* = \begin{cases} 0 & \text{for} \quad v_i^{\text{slip}} = 0 \\ \mu_s & \text{for} \quad 0 < |v_i^{\text{slip}}| < V \\ \mu_k & \text{for} \quad V \leq |v_i^{\text{slip}}| \end{cases}$$

where v_i^{slip} is the slip velocity of the i-th node with respect to the plate and V is the friction transition velocity, that determines the threshold between static and dynamic frictions. The frictional force f_i^{friction} is in the opposite direction to the slip velocity of the node with respect to the plate's surface.

IV. Parameter Estimation

We show how to estimate the viscoelastic parameters of a real deformable object by experiments.

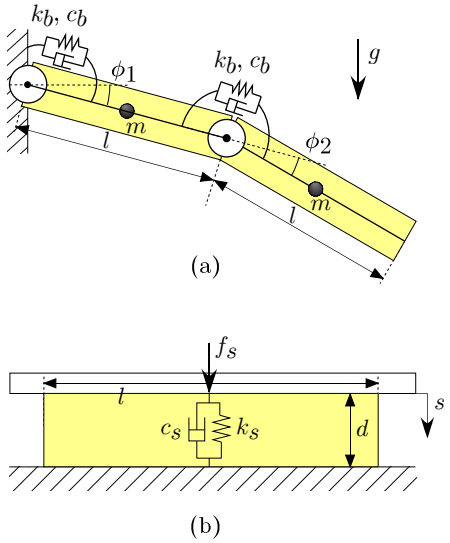

Fig. 8. Parameter estimation model.

A. How to Estimate Parameters

Viscoelasticity in Bending: Fig. 8(a) shows the side view of the model utilized to estimate the viscoelasticity in bending. This model is composed of two links and two bending joints. One joint connects the left tip to the wall and the other joint connects the two links, leaving the right tip free; thus, it is deformed by gravity. This deformation is approximated by two angles: ϕ_1 and ϕ_2, which denote the angle of the two bending joints, the one between the wall and the left tip of the model, and the one between the two links, respectively. The equation of motion of this model is expressed as follows,

$$\begin{bmatrix}\dot{\phi}_2 & \phi_2\end{bmatrix}\begin{bmatrix}c_b\\ k_b\end{bmatrix} = \frac{1}{2}mgl\cos(\phi_1+\phi_2) - \frac{1}{4}ml^2\ddot{\phi}_2 - \frac{1}{4}(1+2\cos\phi_2)\,ml^2\ddot{\phi}_1 \ . \tag{3}$$

Using the sampling data in t_i $(i=1,\ldots,n)$, (3) is expressed by

$$\boldsymbol{A}\boldsymbol{p}_b - \boldsymbol{q} = \boldsymbol{0} \tag{4}$$

where

$$\boldsymbol{A} \triangleq \begin{bmatrix}\dot{\phi}_2(t_1) & \phi_2(t_1)\\ \dot{\phi}_2(t_2) & \phi_2(t_2)\\ \vdots & \vdots\\ \dot{\phi}_2(t_n) & \phi_2(t_n)\end{bmatrix}$$

$$\boldsymbol{p}_b \triangleq \begin{bmatrix}c_b & k_b\end{bmatrix}^{\mathrm{T}}$$

$$\boldsymbol{q} \triangleq \begin{bmatrix}\frac{1}{2}mgl\cos(\phi_1(t_1)+\phi_2(t_1)) - \frac{1}{4}ml^2\ddot{\phi}_2(t_1) - \frac{1}{4}(1+2\cos\phi_2(t_1))\,ml^2\ddot{\phi}_1(t_1)\\ \frac{1}{2}mgl\cos(\phi_1(t_2)+\phi_2(t_2)) - \frac{1}{4}ml^2\ddot{\phi}_2(t_2) - \frac{1}{4}(1+2\cos\phi_2(t_2))\,ml^2\ddot{\phi}_1(t_2)\\ \vdots\\ \frac{1}{2}mgl\cos(\phi_1(t_n)+\phi_2(t_n)) - \frac{1}{4}ml^2\ddot{\phi}_2(t_n) - \frac{1}{4}(1+2\cos\phi_2(t_n))\,ml^2\ddot{\phi}_1(t_n)\end{bmatrix} .$$

From the least squares solution of (4), the viscoelastic parameters $\hat{\boldsymbol{p}}_b \triangleq [\hat{c}_b\ \hat{k}_b]^{\mathrm{T}}$ can be estimated by

$$\hat{\boldsymbol{p}}_b = (\boldsymbol{A}^{\mathrm{T}}\boldsymbol{A})^{-1}\boldsymbol{A}^{\mathrm{T}}\boldsymbol{q} \ . \tag{5}$$

Viscoelasticity in Compression: Fig. 8(b) shows the side view of the model utilized to estimate the viscoelasticity in compression, where one link with a small thickness d is put on a table. The deformation of the link is given by a displacement s, and the viscoelastic parameters in the Kelvin-Voigt model are k_s, and c_s. The contact force f_s applied to the upper surface with area l^2 and the displacement s are utilized in the equation of motion which is expressed as follows,

$$\begin{bmatrix}\dot{s} & s\end{bmatrix}\begin{bmatrix}c_s\\ k_s\end{bmatrix} = f_s \ . \tag{6}$$

Using the sampling data in t_i $(i=1,\ldots,n)$, (6) is expressed by

$$\boldsymbol{B}\boldsymbol{p}_s - \boldsymbol{f}_s = \boldsymbol{0} \tag{7}$$

where

$$\boldsymbol{B} \triangleq \begin{bmatrix}\dot{s}(t_1) & s(t_1)\\ \dot{s}(t_2) & s(t_2)\\ \vdots & \vdots\\ \dot{s}(t_n) & s(t_n)\end{bmatrix}$$

$$\boldsymbol{p}_s \triangleq \begin{bmatrix}c_s & k_s\end{bmatrix}^{\mathrm{T}}$$

$$\boldsymbol{f}_s \triangleq \begin{bmatrix}f_s(t_1) & \cdots & f_s(t_n)\end{bmatrix}^{\mathrm{T}} .$$

From the least squares solution of (7), the viscoelastic parameters $\hat{\boldsymbol{p}}_s \triangleq [\hat{c}_s\ \hat{k}_s]^{\mathrm{T}}$ can be estimated by

$$\hat{\boldsymbol{p}}_s = (\boldsymbol{B}^{\mathrm{T}}\boldsymbol{B})^{-1}\boldsymbol{B}^{\mathrm{T}}\boldsymbol{f}_s \ . \tag{8}$$

Here $\hat{\boldsymbol{p}}_s$ represents the viscoelasticity parameters over the upper surface (l^2). Since in our model we want to describe the viscoelasticity over the lateral surface of the link (ld), we convert $\hat{\boldsymbol{p}}_s$, to obtain $\hat{\boldsymbol{p}}_c \triangleq [\hat{c}_c\ \hat{k}_c]^{\mathrm{T}}$ as

$$\hat{\boldsymbol{p}}_c = \hat{\boldsymbol{p}}_s\,(d/l)^2 \tag{9}$$

which expresses the scaled viscoelasticity for a contact force applied to the lateral surface of the link with area ld and thickness l, based on assumption 4 that the object is isotropic.

B. Parameter Estimation of Real Object

As a real deformable object, a slice of cheese is employed in the experiment since it is an artificial product that can reasonably correspond to assumptions 4, 5, and 6. Based on the model shown in Fig. 7(a), each squared link has a length of $l = 10$ mm, thickness $d = 2.5$ mm, and mass $m = 0.285$ g.

For estimating the viscoelastic parameters in bending, a slice of cheese was cut to get the two link model shown in Fig. 8(a). Actually, its total length is 30 mm and its width is 10 mm, as shown in Fig. 9(a), where the left 10 mm of the object were gripped at the wall portion. We placed three red markers: the first one at the wall boundary, the second one at the middle of the right 20 mm of the object where the virtual joint is located, and the third one at the right tip of the object which is left free. In the initial state, the

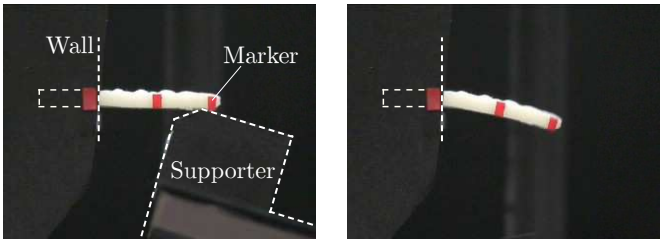

(a) $t = 0.0$ [s] (b) $t = 0.20$ [s]

Fig. 9. Snapshots of the experiment to estimate the viscoelasticity parameters in bending.

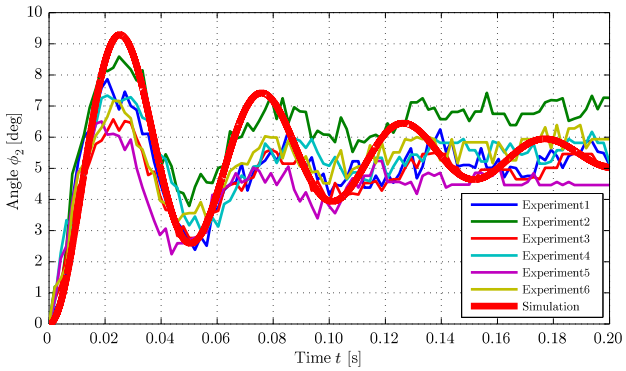

Fig. 10. Angle ϕ_2 with respect to time during the estimation of the viscoelasticity in bending.

cheese is supported as shown in Fig. 9(a), and then released so as to be deformed by gravity as shown in Fig. 9(b). We obtain the joint's angles data $\phi_1(t_i)$ and $\phi_2(t_i)$ $(i = 1, \ldots, n)$ by measuring the markers positions using vision with 480 frames per second. Fig. 10 shows the angle ϕ_2 with respect to time during the deformation by gravity. From these data and (5) with $n = 97$, the parameters $\hat{k}_b = 2.72 \times 10^{-3}$ N·mm/deg and $\hat{c}_b = 4.23 \times 10^{-6}$ N·mm/(deg/s) are obtained. In Fig. 10, the reconstructed result of ϕ_2 using the estimated parameters is overlapped. From this figure, it can be seen that the experimental results and the reconstructed one matched nicely.

For estimating the viscoelastic parameters in compression, a slice of cheese was cut to get the single link model of length $l = 10$ mm, width $l = 10$ mm and thickness $d = 2.5$ mm shown in Fig. 8(b); as shown in Fig. 11 the object is compressed by a parallel jaw gripper actuated by a linear slider. The displacement data $s(t_i)$ is measured by a linear encoder implemented in the slider, and the contact force data $f_s(t_i)$ $(i = 1, \ldots, n)$ is measured by a load cell attached to the parallel jaw gripper. Fig. 12 shows the displacement s and the contact force f_s with respect to time during the deformation by compression. From these data and (8) with $n = 10$, the parameters $\hat{k}_s = 12$ N/mm and $\hat{c}_s = 7.9 \times 10^{-3}$ N/(mm/s) are obtained. Then, $\hat{k}_c = 0.79$ N/mm and $\hat{c}_c = 4.9 \times 10^{-4}$ N/(mm/s) are obtained by the conversion based on (9) . In Fig. 12, the reconstructed result of f_s using the estimated parameters and the displacement in Experiment 1 is overlapped. From this figure, it can be seen that the experimental results and the reconstructed one matched nicely.

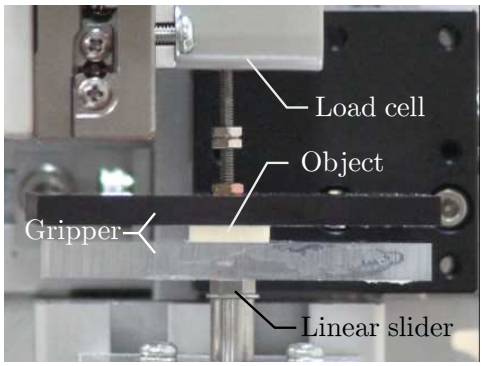

Fig. 11. Snapshot of the experiment to estimate the viscoelasticity parameters in compression.

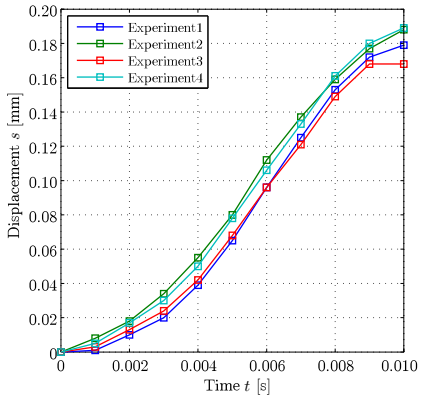

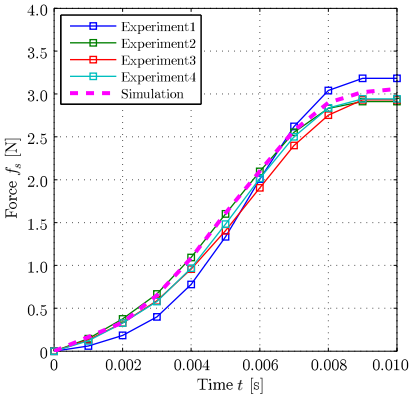

Fig. 12. Displacement s and contact force f_s with respect to time during the estimation of the viscoelasticity in compression.

V. Simulation Analysis

We investigate through simulation analysis, how the object's behavior changes with respect to the given plate motion and obtain the optimal plate motion leading to the maximal angular velocity of the object. We further show that there exists an optimal friction coefficient that yields the maximal angular velocity of the object.

A. Settings

A commercially available slice of cheese as shown in Fig. 13(a), is used for simulation analysis. The slice of cheese has a circular shape of radius $r = 40$ mm, thickness $d = 2.5$ mm, and mass $M = 13.6$ g. The simulation software MD

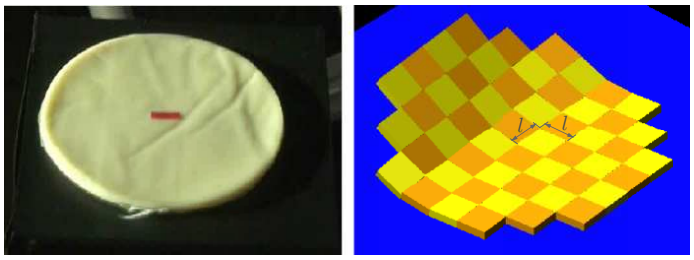

(a) (b)

Fig. 13. The slice of cheese used in the experiments in (a) and the simulation model of a slice of cheese composed of 52 links with $l = 10$ mm in (b).

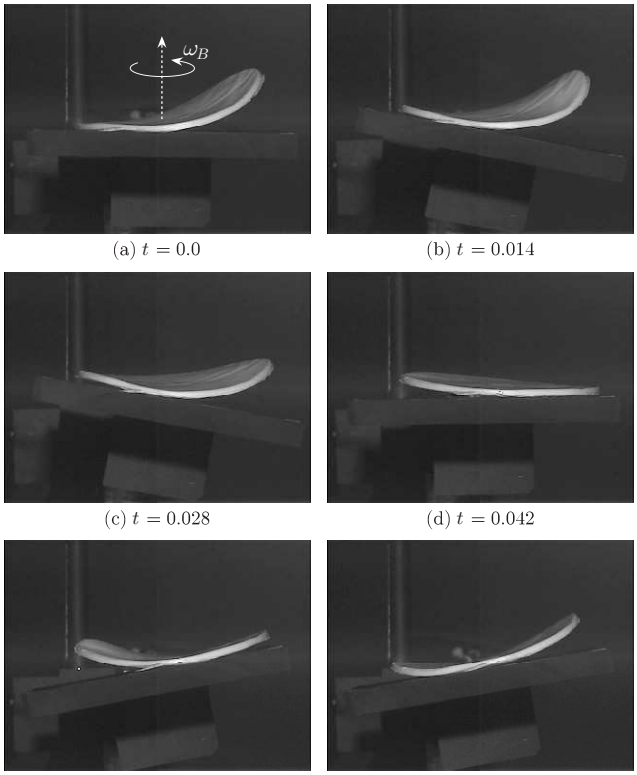

(a) $t = 0.0$ (b) $t = 0.014$
(c) $t = 0.028$ (d) $t = 0.042$
(e) $t = 0.056$ (f) $t = 0.069$

Fig. 14. Snapshots of the experiment using $\omega_p/\omega_n = 2.4$. The object is rotating on the plate with an angular velocity of $\omega_B = 370$ deg/s.

Adams (MSC.Software Corp.) is utilized to compute the dynamic motion of the object. The simulation model as shown in Fig. 13(b) is composed of 52 links with $l = 10$ mm. The four viscoelastic parameters obtained in the previous section are utilized together with the friction's coefficients $\mu_s = 0.75$ and $\mu_k = 0.4$ obtained experimentally and $V = 100$ mm/s. Additionally, $k_{\text{contact}} = 11.86$ N/mm, $c_{\text{contact}} = 7.65 \times 10^{-3}$ N/(mm/s) are given. In order to rotate the object, we give to the plate's two DOFs of motion the following sinusoidal trajectories

$$\Theta(t) = -A_p \sin(\omega_p t) \quad (10)$$

$$X(t) = B_p \sin(\omega_p t) \quad (11)$$

where A_p, B_p, and ω_p denote the rotational amplitude, the linear amplitude, and the angular frequency of the plate motion, respectively.

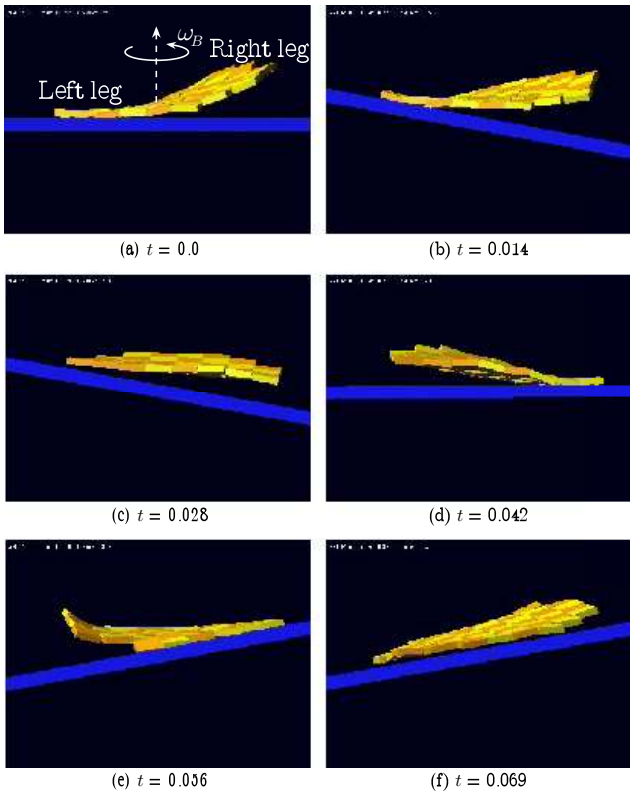

(a) $t = 0.0$ (b) $t = 0.014$
(c) $t = 0.028$ (d) $t = 0.042$
(e) $t = 0.056$ (f) $t = 0.069$

Fig. 15. Snapshots of the simulation using $\omega_p/\omega_n = 2.4$. The object is rotating on the plate with an angular velocity of $\omega_B = 350$ deg/s.

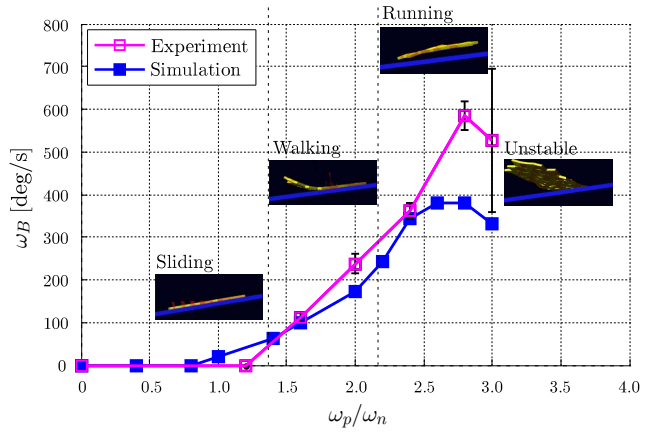

Fig. 16. Angular velocity of the object ω_B with respect to the angular frequency of the plate ω_p/ω_n. The object's behavior changes as bipedal gaits sliding, walking, and running as ω_p/ω_n increases.

B. Analogy to Bipedal Gaits

Fig. 14 and Fig. 15 show the experimental result and the simulation result[2], respectively, with $A_p = 12$ deg, $B_p = 3$ mm, and $\omega_p = 12 \times 2\pi$ rad/s. From these figures, it can be seen that the dynamic behavior in simulation and that in the experiment qualitatively correspond to each other. Fig. 16 shows the relationship between the angular frequency of the plate ω_p and the angular velocity of the object ω_B in simulation and experiment, where ω_p is normalized by $\omega_n = 10\pi$

[2]The video attachment file of this paper shows experiments and the simulations illustrating the object's behaviors of rotation on the plate.

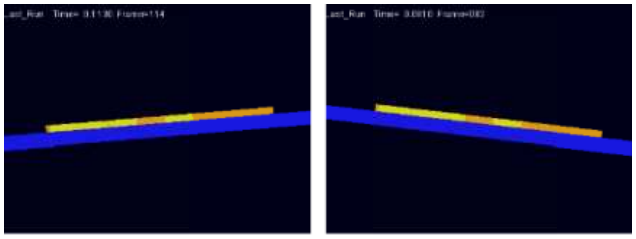

(a) Sliding ($\omega_p/\omega_n = 1.0$)

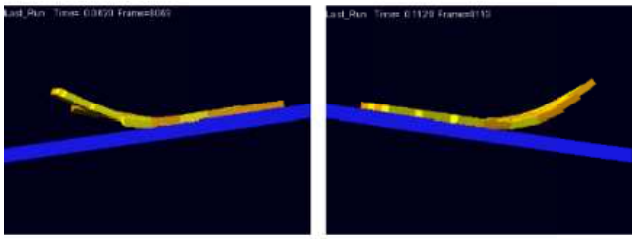

(b) Walking ($\omega_p/\omega_n = 2.0$)

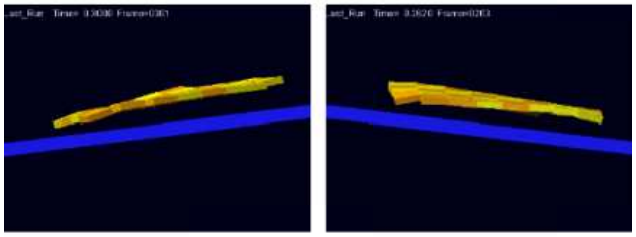

(c) Running ($\omega_p/\omega_n = 2.6$)

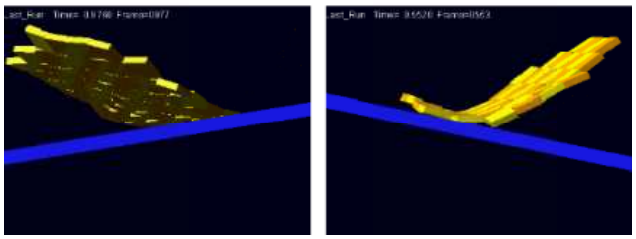

(d) Unstable ($\omega_p/\omega_n = 3.0$)

Fig. 17. Analogy to bipedal gaits: if the whole object is separated into two parts by its center and regarding each of these parts as left leg and right leg, as shown in Fig. 15(a); then the object's behavior can be described with an analogy to bipedal gaits: in (a) sliding (both legs always make contact with the floor), in (b) walking (at least one leg makes contact with the floor), and in (c) running (both legs float at the same time). Failures are defined as those cases in which the object's center slips more than 10 mm or when the object turns over (d).

rad/s which is the first order natural angular frequency of the object in bending, that is the frequency with which the object bends up and down freely, without any external forces nor restraints. It can be seen that the maximal angular velocity of the object is produced with $\omega_p/\omega_n \approx 2.8$ in both simulation and experiment. This comparison between the experimental and simulation results supports the validity of the parameter estimation.

Here, it can be noted that the object's behavior changes with respect to ω_p. An interesting observation is that, if the whole object is separated into two parts by its center, as shown in Fig. 15(a), and regarding each of these parts as left leg and right leg; then the object's behavior can be described with an analogy to bipedal gaits as follows: sliding (both legs always make contact with the floor), as shown in Fig. 17(a), walking (at least one leg makes contact with the floor), as shown in Fig. 17(b), and running (both legs float at the same time), as shown in Fig. 17(c). The transition of these behaviors as ω_p increases is as shown in Fig. 16. The maximal angular velocity is achieved in the running phase, which is also dynamically stable. Finally, for a larger ω_p, the object becomes unstable and it cannot rotate anymore, as shown in Fig. 17(d). We define failures as those cases in which the object's center slips more than 10 mm or when the object turns over.

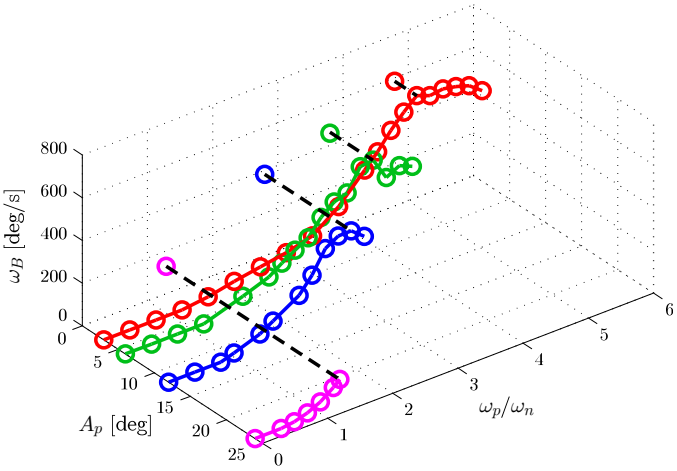

Fig. 18. Relationship between the plate's rotational amplitude A_p, the plate's angular frequency normalized by the first order natural frequency of the object in bending ω_p/ω_n, and the angular velocity of the object ω_B with $B_p = 3$ mm.

C. Optimal Plate Motion

The simulation results in Fig. 18 show the relationship between the rotational amplitude of the plate A_p, the angular frequency of the plate ω_p normalized by ω_n, and the angular velocity of the object ω_B with $B_p = 3$ mm. In this case, changing the value of the translational amplitude B_p does not have a significant effect on the object's angular velocity. The dashed lines indicate the maximal angular velocity $\omega_{B\,\max}$ for each A_p, projected onto the ω_p/ω_n-ω_B plane. Each curve stops when the object became unstable and failed to rotate, which we define in the previous subsection, as shown in Fig. 17(d). If the robot can generate a high frequency motion of the plate e.g. $\omega_p/\omega_n = 5$, the object will be able to rotate faster more stably with a small angular amplitude of the plate rather than with a large one. It can be intuitively understood that a small angular amplitude A_p contributes to the stability of the rotating object. From Fig. 18, the optimal combination of A_p and ω_p can be obtained, which leads to the maximal angular velocity of the object, under the given specification of the robot system.

Figs. 19(a)–(h) show the relationship between the rotational amplitude of the plate A_p, the angular acceleration of the plate $A_p\omega_p^2$, and the angular velocity of the object ω_B, where the natural angular frequency of the object is: (a) $\omega_n = 1.4\pi$ rad/s, (b) $\omega_n = 3.5\pi$ rad/s, (c) $\omega_n = 7.5\pi$ rad/s, (d) $\omega_n = 10\pi$ rad/s, (e) $\omega_n = 15\pi$ rad/s, (f) $\omega_n = 23\pi$ rad/s, (g) $\omega_n = 33\pi$ rad/s, and (h) $\omega_n = 320\pi$ rad/s, with $B_p = 3$ mm. The value of ω_n is changed by modifying the elasticity of the object for the same mass. In Fig. 19, the □, △, and ◯ denote the

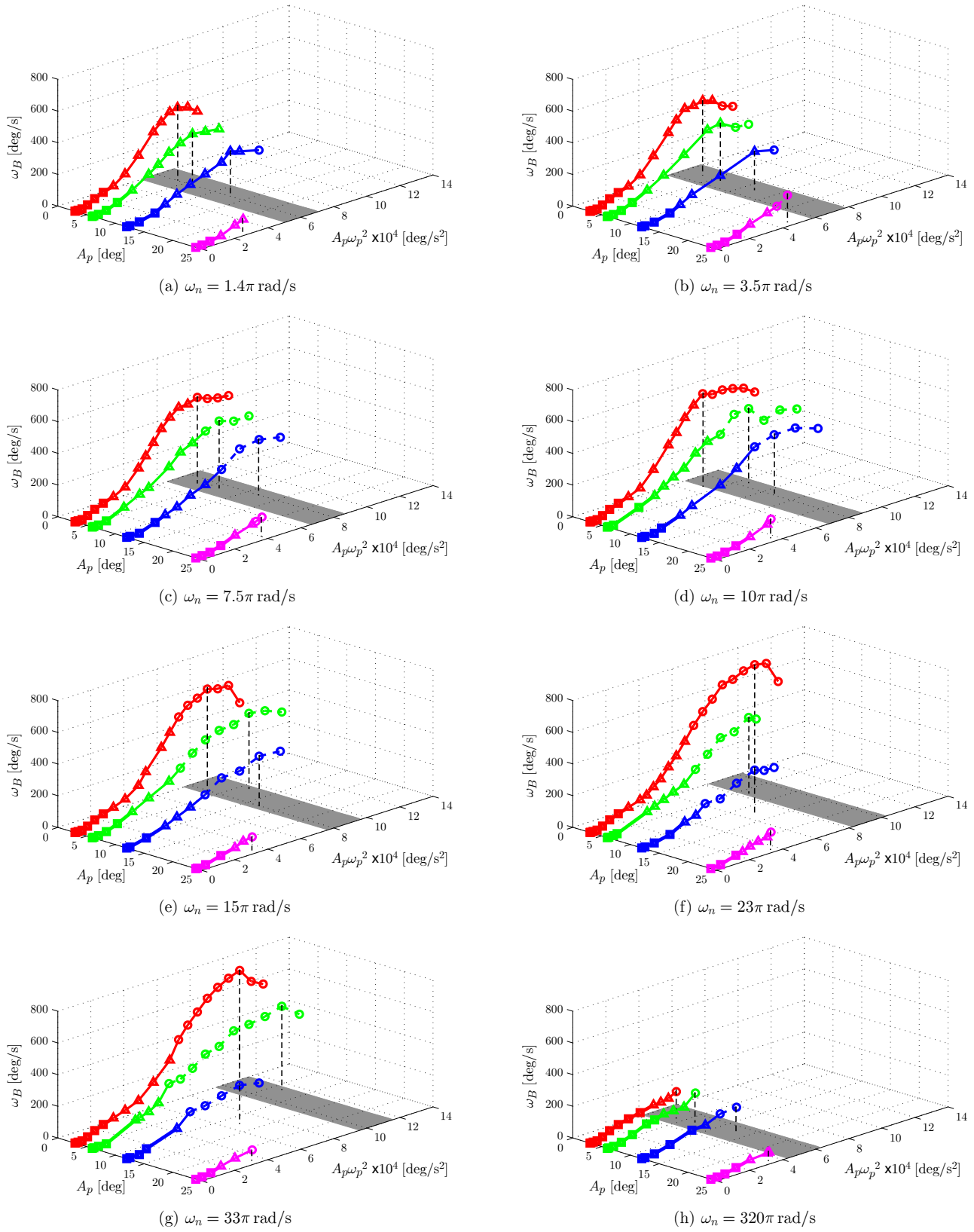

(a) $\omega_n = 1.4\pi$ rad/s (b) $\omega_n = 3.5\pi$ rad/s

(c) $\omega_n = 7.5\pi$ rad/s (d) $\omega_n = 10\pi$ rad/s

(e) $\omega_n = 15\pi$ rad/s (f) $\omega_n = 23\pi$ rad/s

(g) $\omega_n = 33\pi$ rad/s (h) $\omega_n = 320\pi$ rad/s

Fig. 19. Relationship between the plate's rotational amplitude A_p, the plate's angular acceleration $A_p\omega_p^2$, and the angular velocity of the object ω_B with $B_p = 3$ mm. The object's behavior changes with respect to the plate's angular acceleration, from sliding □, to walking △, and to running ◯.

object's sliding, walking, and running phases, respectively. The dashed lines indicate the maximal angular velocity $\omega_{B\,\max}$ for each A_p, projected onto the A_p-$A_p\omega_B^2$ plane. As shown in Fig. 19(h), the object with the highest stiffness becomes

unstable even with a low acceleration of the plate. Thus, the maximal angular velocity of the object $\omega_{B\max}$ is smaller than that of the softer objects in Figs. 19(a)–(g). This corresponds to the experimental results as shown in Fig. 4 and Fig. 6. From Figs. 19(a)–(h), it can be confirmed that the optimal angular acceleration $A_p\omega_p^2$ is uniquely determined for each of the deformable objects, as indicated by the shaded area, while the maximal angular velocity of the object $\omega_{B\max}$ changes depending on how large the amplitude A_p is chosen. It can be noted that for $A_p = 24$ deg, the maximal angular velocity of each of the objects $\omega_{B\max}$ in Figs. 19(a)–(h), is not within the shaded area, since the objects fall from the plate or turn over before achieving a fast rotation. This means that the plate's amplitude is too large to stably manipulate these objects. Furthermore, it can be seen that for $A_p = 12$ deg, the maximal angular velocity of each of the harder objects in Figs. 19(f)–(h) is not within the shaded area. This means that the plate's amplitude $A_p = 12$ deg is still too large to allow these objects to rotate stably on the plate. As shown in Figs. 19(c)–(h), the maximal angular velocity of the object $\omega_{B\max}$ is produced in the running phase. This means that, to rotate the object faster, the plate needs a large enough acceleration to push up the object so that it can run and turn. In this case, the object mainly rotates in the air by utilizing the inertial effect around its center of mass. However, as shown in Fig. 19(a) and (b), the maximal angular velocity of the object is produced in the walking phase. The reason is that the object is too soft, hence the object is greatly deformed, and as a result, it is folded in two before it starts to run. Thus, although the object's behavior differs, an appropriate angular acceleration of the plate is essential to generate a fast and stable rotation of the deformable object. Based on the above results, we can estimate the specifications of the robot's actuators needed for this manipulation scheme.

D. Optimal Friction Coefficients

The simulation results in Fig. 20 show the relationship between the angular acceleration of the plate $A_p\omega_p^2$, the friction angle between the plate and the object $\alpha = \tan^{-1}(\mu_s)$ and the angular velocity of the object ω_B, for a plate's rotational amplitude $A_p = 3$ deg, translational amplitude $B_p = 3$ mm and $\omega_n = 10\pi$ rad/s. The □, △, and ◯ denote the object's sliding, walking, and running phases, respectively. Here, it must be pointed out that not only the static coefficient of friction μ_s, but also the dynamic coefficient of friction μ_k changes and it does it proportionally to μ_s, that is $\mu_k = \beta\mu_s$, where $\beta = 0.53$ is constant.

The friction's influence in the object's angular velocity ω_B, as shown in Fig. 20, can also be explained with the analogy to bipedal gaits. When the friction angle α is around 0 deg, the object cannot rotate fast because the moment contributing to rotation n_+ cannot be generated. This corresponds with a slippery floor for a biped's gait. In the other extreme, when the friction angle α is around 80 deg, the object also cannot rotate fast. This is because the frictional force perpendicular to the plate's translational motion X increases as well as the one parallel to X. Therefore the object will eventually not be able to rotate on the plate, as the friction angle α approaches

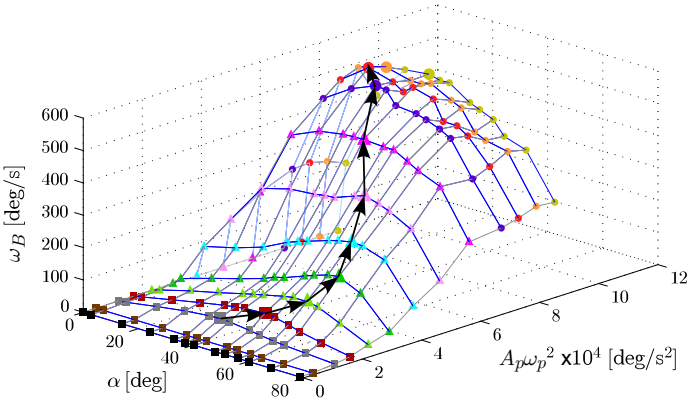

Fig. 20. Relationship between the friction angle between the plate and the object α, the angular acceleration of the plate $A_p\omega_p^2$, and the angular velocity of the object ω_B with $A_p = 3$ deg, $B_p = 3$ mm and $\omega_n = 10\pi$ rad/s. The optimal friction angle depends on the object's sliding □, walking △, and running gaits ◯, as denoted by the arrows.

90 deg. This corresponds with a sticky floor, where a biped can hardly step. Thus the optimal friction angle leading to the maximal angular velocity $\omega_{B\max}$ exists in an intermediate friction value. For a small $A_p\omega_p^2$ as in the sliding phase □, the object keeps full contact with the plate and no deformation occurs. In this case, both the contributing moment n_+ and the braking moment n_- are generated, as shown in Fig. 2(c), and the optimal friction angle is around 40 deg. In the walking phase △, the braking moment n_- decreases due to the object's deformation, as explained in Fig. 2(d). Therefore the optimal friction angle moves to a larger one, around 60 deg, so as to increase the contributing moment n_+ without overcoming the inertial force. For a larger $A_p\omega_p^2$ as in the running phase ◯, the object's contact area during rotation is drastically reduced. Thus the object rotates faster by the inertial effect while floating on the air for most of the time, without making contact with the plate. In this case, a large friction brakes the object's rotation at the instants of time it makes contact with the plate. To avoid this braking, the optimal friction angle moves to a smaller one, around 30 deg. As it was explained, the optimal friction angle denoted by arrows in Fig. 20, depends on the object's sliding, walking, and running gaits.

Furthermore, the optimal angular acceleration $A_p\omega_p^2$ is obtained around 8 deg/s^2, regardless of the friction angle α. This angular acceleration is the same as the one obtained in Fig. 19(d). This confirms that an appropriate plate's angular acceleration is the most important factor for a fast object's rotation.

VI. Conclusion

This paper discussed a dynamic nonprehensile manipulation strategy for rotating a thin deformable object on a rigid two DOFs plate. The main results of this paper are summarized as follows:

- We explained how a deformable object rotates faster than a rigid one on a plate. The bending motion generated by the plate's rotational motion reduces the braking moment, thus contributing to a faster rotation.

- We introduced a model to approximate the dynamic behavior of a deformable object, where the object is composed of multiple nodes and three DOFs joint units with viscoelasticity.
- We showed how to estimate the object's viscoelastic parameters by experiment, and showed the simulation and experimental results to validate the introduced model. Dynamic behaviors in both simulation and experiment correspond to each other qualitatively.
- We discovered through simulation analysis that the transition of the object's rotational behavior with respect to the plate frequency, mimics either a sliding, walking, or running gait of a biped.
- We obtained the optimal plate motion leading to the object's maximal angular velocity and revealed that the angular acceleration of the plate is the most important factor for dynamically stable and fast object rotation.
- We investigated how the friction between the plate and the object influences the object's angular velocity, and showed that the optimal friction coefficient depends on the object's gait.

In this paper, we showed the motion analysis by focusing on the rotation of a deformable object. However, the proposed manipulation scheme has the potential to produce various types of object's locomotions. If we change the sinusoidal wave's phase and period combination of the translational and the rotational motion of the plate, then object's locomotion may become diverse, such as taking steps forward, back, and turning. In future work, we would like to discuss such a marionette-like manipulation toward the simultaneous control of the position and the orientation of a deformable object.

REFERENCES

[1] N. Furukawa, A. Namiki, S. Taku, and M. Ishikawa, "Dynamic regrasping using a high-speed multifingered hand and a high-speed vision system," in *Proc. IEEE Int. Conf. Robot. Autom.*, 2006, pp. 181–187.

[2] M. Higashimori, M. Kimura, I. Ishii, and M. Kaneko, "Dynamic capturing strategy for a 2-D stick-shaped object based on friction independent collision," *IEEE Trans. Robot.*, vol. 23, pp. 541–552, Jun. 2007.

[3] H. Arai and O. Khatib, "Experiments with dynamic skills," in *Proc. Jpn.-USA Symp. Flexible Autom.*, 1994, pp. 81–84.

[4] K. M. Lynch, N. Shiroma, H. Arai, and K. Tanie, "The roles of shape and motion in dynamic manipulation, the butterfly example," in *Proc. IEEE Int. Conf. Robot. Autom.*, 1998, pp. 1958–1963.

[5] K. M. Lynch and M. T. Mason, "Dynamic nonprehensile manipulation: controllability, planning, and experiments," *Int. J. Robot. Res.*, vol. 18, no. 8, pp. 64–92, 1999.

[6] A. Amagai and K. Takase, "Implementation of dynamic manipulation with visual feedback and its application to pick and place task," in *Proc. IEEE Int. Symp. Assem. Task Planning*, 2001, pp. 344–350.

[7] D. Reznik, and J. Canny, "A flat rigid plate is a universal planar manipulator," in *Proc. IEEE Int. Conf. Robot. Autom.*, 1998, pp. 1471–1477.

[8] D. Reznik, E. Moshkovich, and J. Canny, "Building a universal planar manipulator," in *Proc. Workshop Dist. Manip. at Int. Conf. Robot. Autom.*, 1999.

[9] D. Reznik and J. Canny, "C'mon part, do the local motion!," in *Proc. IEEE Int. Conf. Robot. Autom.*, 2001, pp. 2235–2242.

[10] K. F. Böhringer, B. Donald, and N. MacDonald, "Sensorless manipulation using massively parallel microfabricated actuator arrays," in *Proc. IEEE Int. Conf. Robot. Autom.*, vol. 1, 1994, pp. 826–833.

[11] K. F. Böhringer, V. Bhatt, and K. Goldberg, "Sensorless manipulation using transverse vibrations of a plate," in *Proc. IEEE Int. Conf. Robot. Autom.*, 1995, pp. 1989–1986.

[12] K. F. Böhringer, K. Goldberg, M. Cohn, R. Howe, and A. Pisano, "Parallel microassembly with electrostatic force fields," in *Proc. IEEE Int. Conf. Robot. Autom.*, vol. 2, 1998, pp. 1204–1211.

[13] T. Vose, P. Umbanhowar, and K. M. Lynch, "Friction-induced velocity fields for point parts sliding on a rigid oscillated plate," *Int. J. Robot. Res.*, vol. 28, no. 8, pp. 1020–1039, Aug. 2009.

[14] T. Vose, P. Umbanhowar, and K. M. Lynch, "Friction-induced lines of attraction and repulsion for parts sliding on a oscillated plate," *IEEE Trans. Autom. Sci. Eng.*, vol. 6, pp. 685–699, Oct. 2009.

[15] T. Vose, P. Umbanhowar, and K. M. Lynch, "Toward the set of frictional velocity fields generable by 6-degree-of-freedom oscillatory motion of a rigid plate," in *Proc. IEEE Int. Conf. Robot. Autom.*, 2010, pp. 540–547.

[16] P. M. Taylor eds., *Sensory Robotics for the Handling of Limp Materials*. Springer-Verlag, 1990, pp. 3–138.

[17] H. Wakamatsu, S. Hirai, and K. Iwata, "Static analysis of deformable object grasping based on bounded force closure," in *Proc. IEEE Int. Conf. Robot. Autom.*, 1996, pp. 3324–3329.

[18] D. Sun, Y. Liu, and J. K. Mills, "Cooperative control of a two-Manipulator system handling a general flexible object," in *Proc. IEEE/RSJ Int. Conf. Intell. Robots and Syst.*, 1997, pp. 5–10.

[19] M. M. Howard and G. A. Bekey, "Recursive learning for deformable object manipulation," in *Proc. Adv. Robot.*, 1997, pp. 939–944.

[20] S. Garg and A. Dutta, "Grasping and manipulation of deformable objects based on internal force requirements," *Int. J. Adv. Robot. Syst.*, vol. 3, no. 2, pp. 107–114, 2006.

[21] H. Wakamatsu, E. Arai, and S. Hirai, "Knotting/unknotting manipulation of deformable objects," *Int. J. Robot. Res.*, vol. 25, no. 4, pp. 371–395, 2006.

[22] M. Saha and P. Isto, "Manipulation planning for deformable linear objects," *IEEE Trans. Robot.*, vol. 23, pp. 1141–1150, Dec. 2007.

[23] M. Shibata, T. Ota, and S. Hirai, "Wiping motion for deformable object handling," in *Proc. IEEE Int. Conf. Robot. Autom.*, Kobe, Japan, 2009, pp. 134–139.

[24] M. Higashimori, K. Utsumi, Y. Omoto, and M. Kaneko, "Dynamic manipulation inspired by the handling of a pizza peel," *IEEE Trans. Robot.*, vol. 25, pp. 829–838, Aug. 2009.

[25] M. Higashimori, Y. Omoto, and M. Kaneko, "Non-grasp manipulation of deformable object by using pizza handling mechanism," in *Proc. IEEE Int. Conf. Robot. Autom.*, Kobe, Japan, 2009, pp. 120–125.

[26] I. G. Ramirez-Alpizar, M. Higashimori, M. Kaneko, C. Tsai and I. Kao, "Nonprehensile dynamic manipulation of a sheet-like viscoelastic object," in *Proc. IEEE Int. Conf. Robot. Autom.*, Shanghai, China, 2011, pp. 5103–5108.

[27] M. Moore, and J. Wihelms, "Collision detection and response for computer animation," *Comput. Graphics*, vol. 22, no. 4, pp. 289–298, 1988.

Ixchel G. Ramirez-Alpizar received the B.S. degree in electronic engineering from the Universidad Autónoma Metropolitana, Mexico City, Mexico, in 2005, and the M.Eng. degree in electronic and control systems engineering from Shimane University, Shimane, Japan in 2010.

She is currently working toward the Ph.D. degree at the Department of Mechanical Engineering, Graduate School of Engineering, Osaka University, Suita, Japan. Her current research interests include dynamic manipulation and control of deformable objects and high-speed robotics.

Ms. Ramirez-Alpizar is a member of the Robotics Society of Japan and the Japan Society of Mechanical Engineers.

Mitsuru Higashimori received the B.S. degree in systems engineering, the M.S. degree in information engineering, and the Ph. D. degree in artificial complex systems engineering from Hiroshima University, Hiroshima, Japan, in 1996, 1998, and 2006, respectively.

From 1998 to 2002, he was with Toshiba Corporation, Tokyo, Japan. From 2002 to 2006, he was a Research Associate with the Department of Artificial Complex Systems Engineering, Hiroshima University. He is currently an Associate Professor with the Department of Mechanical Engineering, Osaka University, Suita, Japan. His current research interests include manipulation schemes for robot hands and active sensing.

Dr. Higashimori is a member of the Robotics Society of Japan, the Society of Instrument and Control Engineers, and the Japan Society of Mechanical Engineers.

Makoto Kaneko received the B.S. degree in mechanical engineering from Kyushu Institute of Technology, Kitakyushu-shi, Japan, in 1976 and the M.S. and Ph.D. degrees in mechanical engineering from Tokyo University, Tokyo, Japan, in 1978 and 1981, respectively.

From 1981 to 1990, he was a Researcher with the Mechanical Engineering Laboratory, Ministry of International Trade and Industry, Tsukuba Science City, Japan. From 1988 to 1989, he was a Postdoctoral Fellow with the Technical University of Darmstadt, Darmstadt, Germany, where he was involved in a project on space robotics. From 1990 to 1993, he was an Associate Professor of computer science and system engineering with Kyushu Institute of Technology. From November 1991 to January 1992, he was an Invited Professor with the Technical University of Darmstadt. From October 1993 to September 2006, he was a Professor with the Industrial Engineering Department, Hiroshima University, Hiroshima, Japan. Since October 2006, he has been a Professor with the Graduate School of Engineering, Osaka University, Suita, Japan. His current research interests include hyper-human technology, medical diagnosis, high-speed robotics, and human analysis.

Prof. Kaneko has received 19 awards, including the Humboldt Research Award in 1997, the IEEE International Conference on Robotics and Automation Best Manipulation Paper Award in 2000, the IEEE International Symposium on Assembly and Task Planning Outstanding Paper Award in 2001, the IEEE ICRA Best Conference Paper Award, Finalists, in 2003, the IEEE Robotics and Automation Society (RAS) King-Sun Fu Memorial Best Transactions Paper Award in 2003, and the Best Conference Paper Award at the IEEE International Conference on Information Acquisition in 2005. He was a Technical Editor of the IEEE TRANSACTIONS ON ROBOTICS AND AUTOMATION from 1990 to 1994. He is a member of the IEEE Robotics and Automation Society (RAS), the IEEE Systems, Man, and Cybernetics Society (SMC), and the IEEE Industrial Electronics Society. He is also a member of the Japan Society of Mechanical Engineers, the Robotics Society of Japan, and the Japanese Society of Instrumentation and Control Engineers. During 2004-2006, he was the project leader of the 21st Century Centers of Excellence of High-Speed Hyper Human Technology. He was also the Vice President of the IEEE RAS during 2004-2005.

Chia-Hung Dylan Tsai received the B.S. degree from National Taiwan University, Taipei, Taiwan, in 2002, and the Ph.D. degree from State University of New York (SUNY) at Stony Brook, Stony Brook, NY, in 2010.

He is currently a postdoctoral fellow with the Department of Mechanical Engineering, Osaka University, Suita, Japan. His research interests include viscoelasticity, robotic grasping/manipulation, nonlinear modeling, high-speed vision, and non-invasive diagnostic techniques.

Imin Kao received the B.S. degree from the National Chung Hsing University, Taichung, Taiwan, in 1981, and the M.S. and Ph.D. degrees from Stanford University, Stanford, CA, in 1986 and 1990, respectively.

He is a Professor in the Department of Mechanical Engineering, State University of New York (SUNY) at Stony Brook, Stony Brook, where he is the founding Faculty Director of the Information and Technology Studies Undergraduate College. He is currently the Associate Dean of the College of Engineering and Applied Sciences at Stony Brook, Stony Brook. Being the Director of the Systems Engineering and Integration Laboratory at Stony Brook, he conducts research in the areas of robotics, intelligent contact interface, stiffness control, microsystems, MEMS, intelligent fault detection and diagnosis, wafer manufacturing, and wafer slicing using wiresaws.

Dr. Kao is a member of the American Society of Mechanical Engineers. He served as an Associate Editor of the IEEE TRANSACTIONS ON ROBOTICS AND AUTOMATION, as well as the International Journal of Advanced Manufacturing Systems.